

# Integrated frequency-modulated optical parametric oscillator

<https://doi.org/10.1038/s41586-024-07071-2>

Received: 29 June 2023

Accepted: 15 January 2024

Published online: 6 March 2024

 Check for updates

Hubert S. Stokowski<sup>1</sup>, Devin J. Dean<sup>1</sup>, Alexander Y. Hwang<sup>1</sup>, Taewon Park<sup>1,2</sup>,  
Oguz Tolga Celik<sup>1,2</sup>, Timothy P. McKenna<sup>1,3</sup>, Marc Jankowski<sup>1,3</sup>, Carsten Langrock<sup>1</sup>,  
Vahid Ansari<sup>1</sup>, Martin M. Fejer<sup>1</sup> & Amir H. Safavi-Naeini<sup>1</sup>✉

Optical frequency combs have revolutionized precision measurement, time-keeping and molecular spectroscopy<sup>1–7</sup>. A substantial effort has developed around ‘microcombs’: integrating comb-generating technologies into compact photonic platforms<sup>5,7–9</sup>. Current approaches for generating these microcombs involve either the electro-optic<sup>10</sup> or Kerr mechanisms<sup>11</sup>. Despite rapid progress, maintaining high efficiency and wide bandwidth remains challenging. Here we introduce a previously unknown class of microcomb—an integrated device that combines electro-optics and parametric amplification to yield a frequency-modulated optical parametric oscillator (FM-OPO). In contrast to the other solutions, it does not form pulses but maintains operational simplicity and highly efficient pump power use with an output resembling a frequency-modulated laser<sup>12</sup>. We outline the working principles of our device and demonstrate it by fabricating the complete optical system in thin-film lithium niobate. We measure pump-to-comb internal conversion efficiency exceeding 93% (34% out-coupled) over a nearly flat-top spectral distribution spanning about 200 modes (over 1 THz). Compared with an electro-optic comb, the cavity dispersion rather than loss determines the FM-OPO bandwidth, enabling broadband combs with a smaller radio-frequency modulation power. The FM-OPO microcomb offers robust operational dynamics, high efficiency and broad bandwidth, promising compact precision tools for metrology, spectroscopy, telecommunications, sensing and computing.

Optical frequency combs, characterized by their precisely spaced, sharp spectral lines that serve as a ‘frequency ruler’ for light, are indispensable tools in numerous fields, from precision metrology and atomic clocks to high-capacity telecommunications and molecular spectroscopy<sup>3–7</sup>. Fuelled by their potential practical applications, the drive to miniaturize frequency combs into chip-scale integrated devices, known as microcombs, has recently accelerated at a remarkable pace<sup>8</sup>. Conventional optical frequency combs, produced through mode-locked lasers and synchronously pumped optical parametric oscillators (OPOs)<sup>1,2</sup>, are large and require substantial infrastructure, such as complex feedback systems or high-power lasers. As a result, their cost is high, and their use outside laboratory settings is limited. Two principal methods for creating integrated frequency comb sources suitable for smaller, deployable devices have been explored in response. The first involves third-order  $\chi^{(3)}$  or Kerr optical nonlinearity, with successful demonstrations in materials such as silica, silicon nitride, aluminium nitride, silicon carbide and lithium niobate (LN)<sup>13–17</sup>. The second strategy uses the electro-optic (EO) effect, which has been realized in resonant (Fig. 1a) and non-resonant integrated thin-film LN devices<sup>10,18,19</sup>. Despite these remarkable advances, EO and Kerr combs face several challenges. These combs are often limited in their efficiency, exhibit a strong pump background, suffer from limited tunability and display an exponentially decreasing comb line intensity

for the lines distant from the pump. Moreover, Kerr frequency combs demand sophisticated control and become substantially more challenging to operate at a smaller free spectral range (FSR).

In this study, we propose and demonstrate a previously unknown type of microcomb that combines the advantages of both EO and Kerr combs, merging nonlinear optical processes with EO modulation in an integrated device. Specifically, our structure accommodates both optical parametric amplification and phase modulation within a single cavity, thereby facilitating the generation of a frequency-modulated optical parametric oscillator<sup>20,21</sup> (FM-OPO; Fig. 1b). Remarkably, unlike in conventional Kerr and EO combs, the dynamics in our system do not result in pulse formation, making the output more closely resemble that of a frequency-modulated laser. In contrast to a serrodyne approach, the radio-frequency (RF) modulation we use has only a single Fourier component. This strategy maintains the operational simplicity characteristic of EO combs while achieving substantially broader bandwidths than those attainable through modulation alone. Furthermore, our technique gives rise to a flat-top output comb with most lines within 3 dB of the mean, an optimal spectral distribution for many applications, while avoiding unwanted nonlinearities that manifest at large pulse peak powers<sup>22</sup>. Finally, the FM-OPO exhibits impressive efficiency, converting a substantial fraction of the pump light into comb lines while demanding only modest RF power inputs for operation.

<sup>1</sup>Department of Applied Physics and Ginzton Laboratory, Stanford University, Stanford, CA, USA. <sup>2</sup>Department of Electrical Engineering, Stanford University, Stanford, CA, USA. <sup>3</sup>Physics and Informatics Laboratories, NTT Research, Sunnyvale, CA, USA. ✉e-mail: safavi@stanford.edu

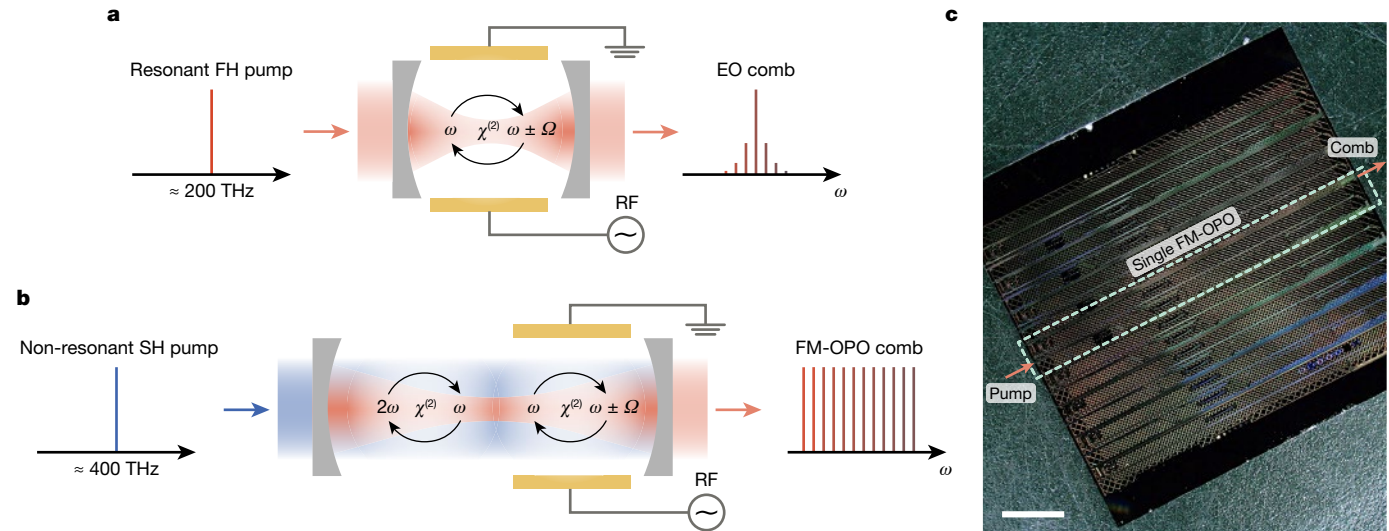


**Fig. 1 | Frequency combs in the EO resonator and FM-OPO.** **a**, In a standard EO comb, an optical resonator conducts EO modulation on a single laser pump. This results in an output of equally spaced lines with intensities that decay exponentially. **b**, The FM-OPO uses the second harmonic (SH) as a pump and emits light at the fundamental frequency. An EO modulator couples the

neighbouring cavity modes, creating an evenly distributed output comb. **c**, The microscope image shows a thin-film LN chip housing eight FM-OPO devices. One device has a footprint of around  $1 \times 10 \text{ mm}^2$  (highlighted with a dashed rectangle). FH, fundamental harmonic. Scale bar, 2 mm.

To demonstrate the integrated FM-OPO, we turn to thin-film LN for its strong second-order optical nonlinearity and EO effect. Thin-film LN has recently emerged as a platform for integrated nanophotonics<sup>23</sup> through demonstrations of efficient EO modulators<sup>24,25</sup>, EO combs<sup>10,18</sup>, periodically poled LN waveguides for frequency conversion<sup>26–28</sup>, quantum light generation<sup>29,30</sup>, resonant second-harmonic generation and OPOs<sup>31–33</sup>, and integration with complex photonic integrated circuits for applications such as laser control<sup>34</sup> and quantum measurements<sup>35</sup>. The above demonstrations are either based on the EO effect that transfers energy between optical modes separated by the RF frequency or the  $\chi^{(2)}$  nonlinearity that can provide broadband gain. Combining these two distinct capabilities forms the foundation for the integrated FM-OPO. Moreover, our choice of LN is motivated by its strong potential for large-scale manufacturability as evidenced by efforts now pursued in industry<sup>36,37</sup>.

## Comb dynamics

Both Kerr and EO comb generation fundamentally rely on mode locking, which subsequently leads to the formation of pulses. However, this process inherently introduces a strong frequency-dependent variation in the intensity of the comb lines that decay exponentially with their offset from the centre. Another considerable challenge posed by pulse formation is the inefficient use of pump power, as a continuous-wave pump overlaps only with a small part of the circulating field. Recent advancements have started to address this issue, mainly by exploiting auxiliary resonances<sup>18,38,39</sup> and using pulsed pumps<sup>40</sup>. Finally, pulse formation leads to large intracavity peak powers that can engage other unwanted nonlinearities and make comb formation challenging in integrated platforms<sup>22</sup>. We discover here that incorporating parametric gain into an EO-modulated cavity leads to a frequency comb without necessitating pulse formation. Our device demonstrates high efficiency, reduced pump background, and spectral flatness. In contrast to the extensive engineering and operation dynamics required for similar results by the Kerr combs, the FM-OPO offers an alternative versatile solution. Moreover, unlike pure EO combs, the FM-OPO requires only modest RF power, enabling scalability and applications in deployable sensors. Despite the modulation being close to the cavity resonance mode spacing, the dynamics of our system strikingly resemble those of a frequency-modulated laser<sup>12,41,42</sup>. As in a frequency-modulated

laser, we will see that the optical frequency of the signal is swept across a bandwidth BW at the rate of the RF modulation  $\Omega$ .

We first consider the situation without any modulation. We assume that we operate the OPO non-degenerately so that it emits signal and idler tones at mode number offsets  $\pm n_{\text{osc}}$  from a central mode with frequency  $\omega_0$  close to half of the pump frequency  $\omega_p/2$ . As we introduce RF modulation at frequency  $\Omega$  characterized by a mode-coupling rate  $M$ , these signal and idler tones are simultaneously subject to gain and modulation. The pairing of these effects around the signal and idler creates conditions that mirror the dynamics of a frequency-modulated laser, in which phase-insensitive gain and modulation coexist.

In a frequency-modulated laser, the limiting behaviour that prevents mode locking arises from a detuning between the FSR of the cavity and the drive frequency  $\Omega$ . The frequency-modulated laser then transitions to chaotic and mode-locked states as this detuning is reduced and the bandwidth is increased to approach the gain bandwidth of the medium or a limit set by the cavity dispersion<sup>12</sup>. The oscillation bandwidth of the FM-OPO is limited by the dispersion of the cavity, characterized by mode frequencies  $\omega_n = \omega_0 + \zeta_1 \times n + \zeta_2/2 \times n^2$ , where  $\zeta_1$  and  $\zeta_2$  are the cavity FSR near  $\omega_0$  and the second-order dispersion, respectively. Under the regime considered, our device avoids the transition to mode-locking behaviour. The signal and idler modes are far separated and experience local FSRs near  $\pm n_{\text{osc}}$  that differ from each other by  $2n_{\text{osc}}\zeta_2$ . Moreover, the parametric nature of the process necessitates the simultaneous formation of combs at both signal and idler frequencies. Therefore, in the assumed non-degenerate regime, there is always effectively a drive detuning when we consider both signal and idler combs. This results in dynamics that closely mirror those of a frequency-modulated laser with detuned driving, in which continuous frequency sweeping is observed rather than pulse formation. The effective bandwidth is given by

$$\text{BW} = 2\Gamma\Omega = \frac{4M\Omega}{n_{\text{osc}}\zeta_2}, \quad (1)$$

where  $\Gamma$  is the modulation index, and the signal and idler tones are frequency modulated as  $a_{s,i}(t) \approx A_{s,i} e^{-i\omega_t t} e^{\mp i\Gamma \sin(\Omega t)} e^{i\omega_p t/2}$ . The bandwidth formula aligns well with the established expression for the frequency-modulated laser bandwidth  $\text{BW} \propto M\Omega/(\Omega - \text{FSR})$  (ref. 12), with the correspondence being that the frequency-modulated laser

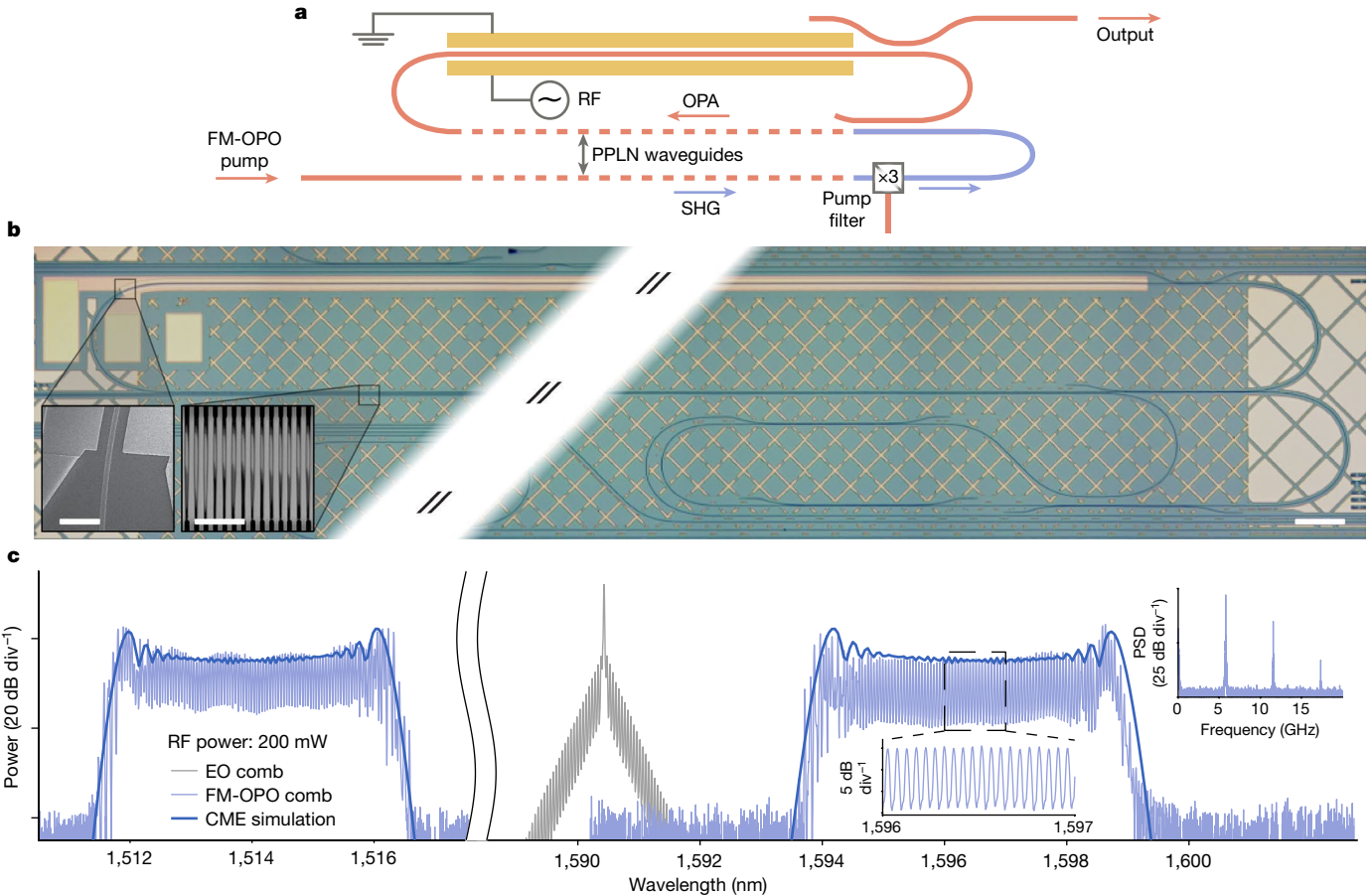


**Fig. 2 | The FM-OPO device.** **a**, The device features a racetrack resonator with an intracavity waveguide coupler, which allows only the fundamental harmonic to resonate while enabling the second harmonic to traverse the device once. The straight section of one racetrack contains a periodically poled waveguide for second-order optical nonlinearity, whereas the other couples to microwaves through on-chip electrodes. A single-pass waveguide on the same chip generates the pump of the OPO at the second-harmonic frequency, which is separated from the input C-band laser light using a series of filters. **b**, The microscope image shows the FM-OPO racetrack resonator, with the centre removed for clarity. The dark lines represent integrated waveguides. The yellow structure atop the racetrack is a gold microelectrode slot waveguide that links with microwaves. The SEM micrograph in the left inset depicts the waveguide between the electrodes. The bottom of the racetrack is periodically poled, as

shown in the second-harmonic microscope image of the poled film in the second inset. The waveguide circuit in the bottom-right corner is a pump-filtering section after the second-harmonic generation (SHG) waveguide. **c**, The output spectrum of the FM-OPO produces approximately 200 unique oscillator modes at the signal and idler frequencies using about 140 mW of input optical power and 200 mW of RF power. The dark-blue line represents a coupled-mode theory simulation result. The bottom-right inset magnifies into the flat area of the comb, whereas the top-right inset shows an RF power spectral density (PSD) of the FM-OPO output, detected using a fast photodiode with peaks at multiples of the cavity FSR. CME, coupled-mode equation; OPA, optical parametric amplification; PPLN, periodically poled LN. Scale bars, 200  $\mu\text{m}$  (**b**, main image); 10  $\mu\text{m}$  (**b**, left inset); and 20  $\mu\text{m}$  (**b**, right inset).

detuning  $\Omega - \text{FSR}$  is replaced by the detuning  $n_{\text{osc}}\zeta_2$  between the drive and local FSR in the FM-OPO. Finally, we note that there are conditions for which the above analysis no longer holds, for example, at (near-) degenerate OPO operation leading to smaller  $n_{\text{osc}}$ , at substantially larger  $M$  or for dispersion-engineered waveguides that may match the local signal or idler FSRs. Bulk phase-modulated OPOs have already been demonstrated<sup>20,21</sup>. In contrast to the FM laser, the FM bandwidth and the gain bandwidth of the FM-OPO are both defined through dispersion engineering. We leave the engineering and study of the dynamics of integrated phase-modulated OPOs in a wider set of operating regimes to future work.

We demonstrate an optical frequency comb generator based on an FM-OPO integrated on a chip (Fig. 1c). The device evenly distributes 11 mW of optical power over 200 comb lines using 140 mW of C-band optical pump power and 200 mW of RF modulation power. Comb lines are spaced by about 5.8 GHz. We base our device on a racetrack resonator in thin-film LN on an insulator with intrinsic quality factors of around  $Q_i \approx 10^6$ . This resonator holds within it an EO modulator, an optical parametric amplifier and a high-efficiency wavelength-selective

coupler that nearly fully transmits the 780 nm pump while keeping the C-band excitation within the cavity. Figure 2a shows a schematic of the device, whereas Fig. 2b shows a microscope image of a single FM-OPO device. The coupler enables our device to operate as a doubly resonant OPO in which the pump passes through the optical parametric amplifier but is non-resonant in the cavity. One straight section has gold electrodes patterned next to it, enabling EO modulation of the cavity (Fig. 2b, left inset). The other straight section of the cavity is a periodically poled LN waveguide that provides parametric gain when pumped with the second harmonic (see Fig. 2b, right inset, for a second-harmonic microscope picture of the poled thin-film LN). In the Methods section, we describe the design and characterization of the waveguides and cavity in detail.

We generate the 780-nm pump on the same chip in a separate periodically poled LN waveguide by second-harmonic generation. We filter out the original pump field through three on-chip filters of the same design as the intracavity coupler. The high second-harmonic generation efficiency enables us to achieve considerable optical pump powers using only a standard commercial C-band laser. Figure 2c shows an example

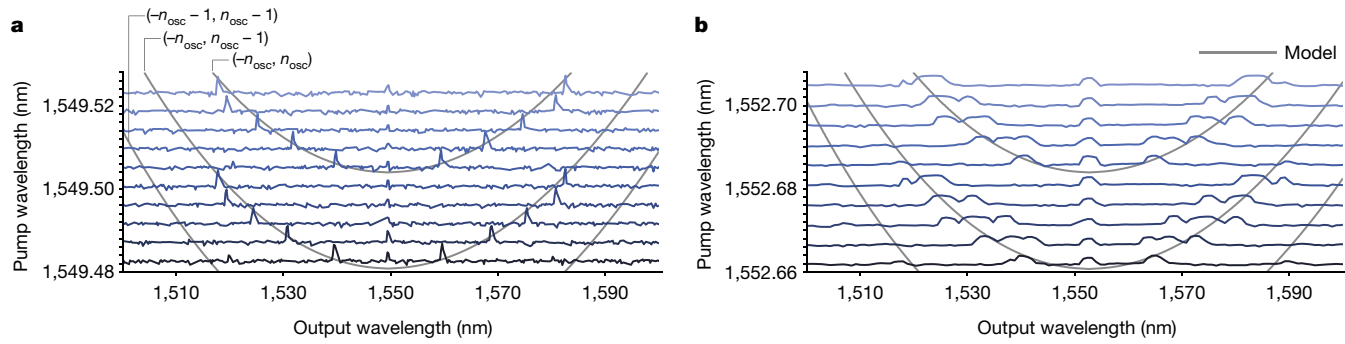


**Fig. 3 | Pump-wavelength tuning of the FM-OPO.** **a**, We examine the pump-wavelength tuning of a doubly resonant OPO. The blue traces relate to optical spectrum analyser measurements. The output wavelength of the DRO is determined by the frequency matching between the signal and idler modes with respect to the pump. The thin grey lines, recurring every 1/2 free spectral

range, correspond to the theoretical model. **b**, The pump-wavelength tuning of the FM-OPO aligns with the pure OPO trend. However, the entire frequency-modulated clusters of modes tune synchronously along the energy-conservation lines. For both **a** and **b**, one division on the y-axis corresponds to a 50-dB change in the detected optical power for each optical spectrum analyser trace.

FM-OPO output spectrum when the device is pumped with around 140 mW of fundamental-harmonic optical power (corresponding to around 100 mW of second-harmonic power) and 200 mW of RF power, equivalent to about 4.5 V peak voltage. We plot an EO comb generated using the same RF power within the same cavity in grey for comparison. We observe a flat comb formation around signal and idler wavelengths and no substantial background from the pump. The measured output aligns with our coupled-mode theory model (thick dark-blue line) described below. The bottom-right inset in Fig. 2c shows individual lines in a flat spectrum spaced by around 5.8 GHz. The observed contrast of around 15 dBm between maxima and minima results from the limited resolution of the optical spectrum analyser rather than the nature of the FM-OPO. The top-right inset in Fig. 2c shows the result of collecting the output using a fast photodetector and an RF spectrum analyser. In the RF spectrum, we observe narrow lines spaced by the multiples of the cavity FSR, resulting from the FM-OPO sweeping over a frequency-dependent output coupler (see the Methods for details).

We can understand nearly all the salient features of the observed spectra in the context of an approximate time-domain coupled-mode theory analysis. We also use this formulation to derive the formula for the comb bandwidth shown in equation (1), which agrees well with observations 4b. We define mode amplitudes  $a_n$  to represent the field amplitudes for the  $n$ th mode around the fundamental-harmonic frequency, where  $n = 0$  corresponds to the fundamental mode closest to half of the pump frequency. In this context,  $b$  represents the amplitude of the second-harmonic pump field. Each mode  $n$  has a natural frequency given by the cavity dispersion with  $\zeta_1/2\pi \approx 5.8$  GHz and  $\zeta_2/2\pi \approx -11$  kHz corresponding to the cavity FSR and the second-order dispersion, respectively. Other key parameters include the laser drive detuning  $\Delta = \omega_p/2 - \omega_0$ , and the RF drive detuning from the FSR  $\delta \equiv \Omega - \zeta_1$ . The mode coupling due to modulation  $M$ , which is proportional to the RF drive voltage, and the nonlinear coupling rate  $g$  provide the critical ingredients for realizing the comb dynamics. We also include the loss rates of the considered field amplitudes,  $\kappa_{a,n}$  and  $\kappa_b$ . The rate  $\kappa_b$  corresponds to that of an extremely lossy single-pass ‘cavity’ and enables us to approximate our DRO in this coupled-mode theory formulation. We derive all of the model parameters from independent simulations, as well as experimental and theoretical analysis (refer to the Methods section and Supplementary Information for more details). The resulting coupled-mode equations are

$$\dot{a}_n = \left[ i \left( \Delta + n\delta - \frac{n^2\zeta_2}{2} \right) - \frac{\kappa_{a,n}}{2} \right] a_n - iM(a_{n-1} + a_{n+1}) - 2iga_{-n}^*b \quad (2)$$

$$b = -\frac{\kappa_b}{2} b - ig \sum_n a_n a_{-n} + i\sqrt{\kappa_b} \beta_{in}. \quad (3)$$

There are two main approximations in these equations. First, we represent the pump field as the excitation of a very lossy mode  $b$ , solutions involving substantial spatial variations of the pump field along the waveguide cannot be represented accurately by this model. Second, we include only coupling between modes  $n$  and  $-n$ —we ignore the weaker coupling between modes with nearby  $n$  numbers. For example, coupling between  $n$  and  $-n+1$  can be present and may become stronger as a function of pump wavelength. Tuning the pump wavelength and consequently the detuning  $\Delta$  over a cavity FSR changes the mode pairs that are amplified (Fig. 3a). The device parameters are shown in Extended Data Table 1.

We tune the output wavelength in the FM-OPO through small adjustments to the pump wavelength, enabling the output to span the full range of the gain spectrum. This tuning is predominantly influenced by the cavity dispersion, mirroring the characteristics observed in an unmodulated OPO<sup>32,43</sup>. We show the OPO tuning behaviour in Fig. 3a. The blue traces correspond to measurements with an optical spectrum analyser, whereas the grey lines present the predicted tuning behaviour based on the waveguide dispersion. The FM-OPO exhibits a similar tuning pattern, as shown in Fig. 3b. Here, the comb clusters closely follow the expected tuning. By adjusting the pump wavelength by 23 pm (or 2.9 GHz), which equates to half of the FSR of the cavity, we can access bandwidth of approximately 70 nm (or 8.7 THz) for both FM-OPO and OPO.

We measure the spectra generated by the FM-OPO using an optical spectrum analyser. We find that the device operates continuously and robustly in a non-degenerate mode at around  $n_{osc} \approx 800$ . In this regime, we expect equation (1) to hold to high accuracy. We pump the device at 1,554 nm with about 140 mW. We step the EO coupling rate of the 5.8-GHz EO modulation between 0 MHz and around 510 MHz by varying the RF power supplied to the chip. As shown in Fig. 4a, we observe a frequency comb develop. Several additional comb clusters labelled  $(-n_{osc} + 1, n_{osc})$  and  $(-n_{osc} + 1, n_{osc} + 1)$  appear at a drive exceeding  $M/2\pi \approx 360$  MHz. Although the single-cluster comb states that are generated for  $M$  below 250 MHz are easier to understand and model, and will likely be more useful in a practical system, we also present the states that arise at larger values of  $M$ , and that result in multiple FM-OPO clusters. These are predicted by our theoretical analysis and described in more detail in the Methods. We plot only the signal combs (blue detuned) and omit the idler combs (red detuned) for clarity; we provide full spectra in Extended Data Fig. 8. The measured spectral peak at around 1,554 nm corresponds to a slight leakage of the

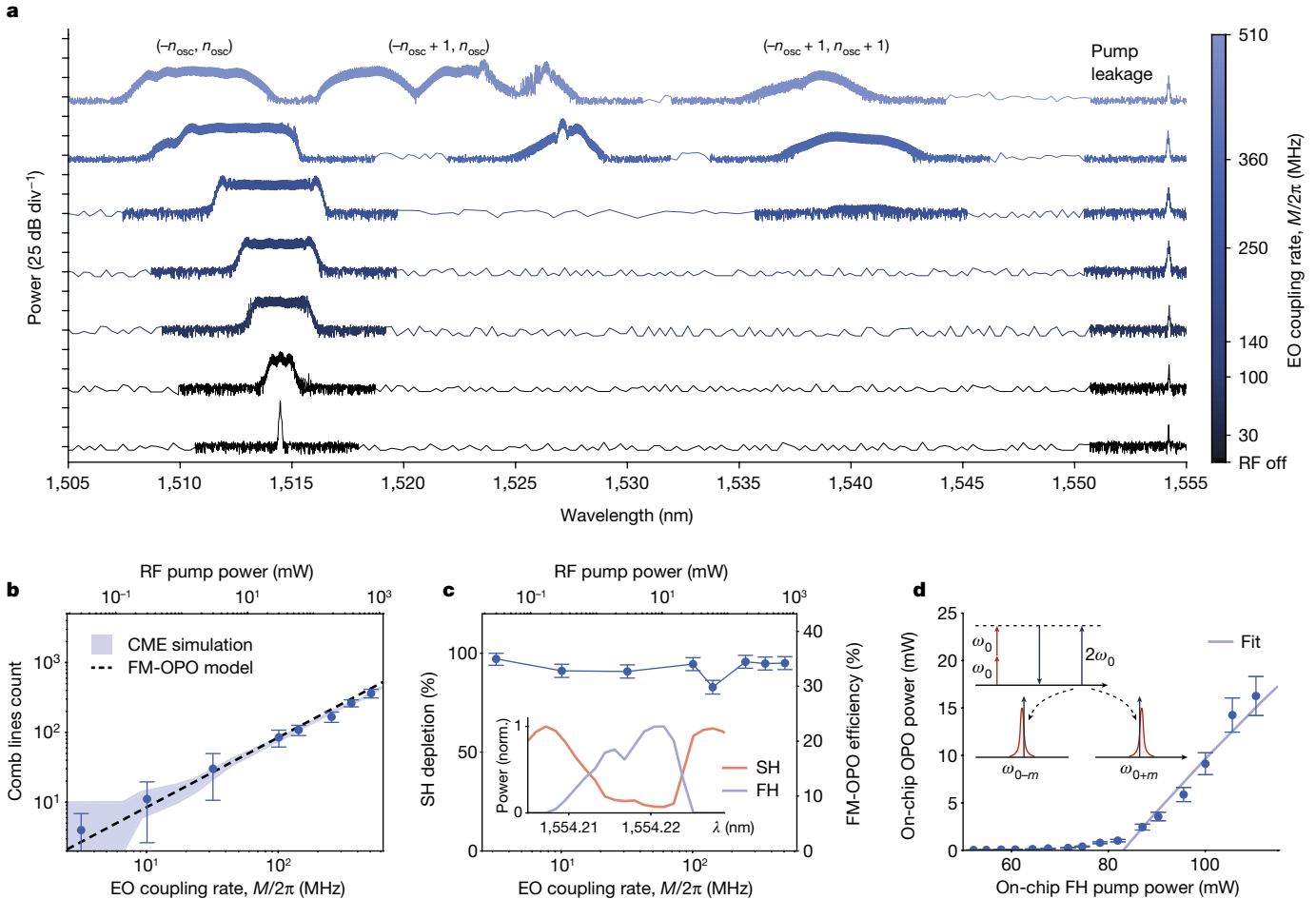


**Fig. 4 | Power tunability of the FM-OPO.** **a**, Evolution of combs with the EO drive. As the EO coupling increases, we observe comb growth and the emergence of secondary combs that couple  $(-n_{\text{osc}} + m, n_{\text{osc}})$  modes, aligning with several grey lines in Fig. 3. We combine high-resolution (approximately 20 pm) measurements from areas with detectable signals and low-resolution readings from the rest of the range. We primarily focus on the signal around 1,515 nm for simplicity. The peak around 1,554 nm is because of a minor leakage of the initial pump into the cavity. **b**, The maximum count of individual oscillating lines in the FM-OPO as a function of EO coupling. The faint blue region corresponds to the prediction from the coupled-mode theory. We plot the comb count predicted with the FM-OPO theory with a dashed line. **c**, We measure the depletion of the

FM-OPO optical pump of around 93%, corresponding to the conversion efficiency of around 34%. The inset shows the normalized second-harmonic generation pump (orange) and FM-OPO (blue) when changing the pump wavelength at  $M/2\pi \approx 30$  MHz. The contrast between the second-harmonic maximum and minimum defines depletion. **d**, The output power of the pure OPO as a function of the pump power at the fundamental-harmonic frequency. The pump initially generates a second harmonic in a single-pass waveguide that later drives the OPO. A line fitting to the data shows a nonlinear coupling rate  $g/2\pi$  of approximately 12 kHz. We describe the displayed measurement and simulation uncertainties in the Methods.

original fundamental-harmonic pump into the cavity. We count the number of generated lines within the 3 dB bandwidth of the mean comb power and plot this in Fig. 4b. We observe good agreement between the data, numerical solution of the coupled-mode equations (2) and (3) (blue-shaded region) and the analytical expression for the FM-OPO given by equation (1) (dashed line). At the highest EO modulation rate of around 1.2 W, we observe more than 1,000 comb lines oscillating together within  $\sim 30$  dB from the flat-top mean power (see Extended Data Fig. 8e for the full spectrum).

The FM-OPO operates with high efficiency, converting around 34% of the input second-harmonic light into comb lines. First, the intracavity conversion efficiency is high, exceeding 90%, based on the pump depletion measurement in Fig. 4c. We chose to use depletion because it is self-calibrating and enables us to calculate the efficiency based on the contrast between the measured maxima and minima of the normalized second-harmonic power (see the Supplementary Information for details), visible when tuning the pump wavelength, as shown in the inset. Next, the intracavity comb is out-coupled with the cavity escape efficiency  $\eta_a \approx 0.36$ , which limits the total efficiency of our device. Note

that the depletion and the conversion efficiency do not depend on the RF drive strength. However, the efficiency depends on the optical pump power and is maximized at around four times the threshold. The output power of the FM-OPO resembles a typical behaviour of an unmodulated OPO in Fig. 4d, in which we observe a threshold of about 47 mW second-harmonic power and nonlinear coupling rate  $g/2\pi \approx 12$  kHz, lower than the predicted 67 kHz, which we attribute to operating at non-perfect phase matching  $\Delta k \neq 0$ . The low power requirements of our device enable direct integration with chip-based lasers<sup>35,44,45</sup> to build self-contained comb generators.

## Discussion

We have successfully demonstrated a new type of integrated comb generator and established its fundamental operating principles. Our device demonstrates exceptional brightness, flatness and efficiency while retaining robust operational dynamics. Increasing the bandwidth and using the nonlinearities of LN will enable  $f-2f$  locking<sup>46</sup>, leading to a truly coherent frequency comb in the stricter sense. Group velocity matching

signal and idler will enable engineering parametric gain bandwidth to cover as much as 3–4 μm (ref. 47), expanding the use of the FM-OPO in mid-infrared spectroscopy. Given that our initial demonstration still has the potential for marked improvements in optical bandwidth by dispersion engineering, RF power consumption by resonant enhancement and optical conversion efficiency by improved out-coupling, this breakthrough opens the door to a new class of deployable optical frequency combs. For the application of these combs to the problems of spectroscopy, the versatility of the LN material platform allows for spectral coverage from blue light<sup>48</sup> into the mid-infrared<sup>27,47</sup>, enabling their use in fields such as medical diagnostics<sup>49</sup>, process control in agriculture, food production and various industrial sectors<sup>50,51</sup>. Although the comb teeth spacing of our current devices is around 5.8 GHz, our platform can achieve an FSR of 50 GHz to meet telecom standards and even exceed 100 GHz, given established modulators<sup>24</sup>. Therefore, we anticipate flat-top combs generated with FM-OPOs to find applications as sources in fibre communication systems. Moreover, they are invaluable for ranging applications using FMCW LiDAR<sup>52</sup>.

## Online content

Any methods, additional references, Nature Portfolio reporting summaries, source data, extended data, supplementary information, acknowledgements, peer review information; details of author contributions and competing interests; and statements of data and code availability are available at <https://doi.org/10.1038/s41586-024-07071-2>.

1. Jones, D. J. et al. Carrier-envelope phase control of femtosecond mode-locked lasers and direct optical frequency synthesis. *Science* **288**, 635–639 (2000).
2. Udem, Th., Holzwarth, R. & Hänsch, T. W. Optical frequency metrology. *Nature* **416**, 233–237 (2002).
3. Diddams, S. A., Vahala, K. & Udem, T. Optical frequency combs: coherently uniting the electromagnetic spectrum. *Science* **369**, eaay3676 (2020).
4. Coddington, I., Newbury, N. & Swann, W. Dual-comb spectroscopy. *Optica* **3**, 414–426 (2016).
5. Suh, M.-G., Yang, Q.-F., Yang, K. Y., Yi, X. & Vahala, K. J. Microresonator soliton dual-comb spectroscopy. *Science* **354**, 600–603 (2016).
6. Picqué, N. & Hänsch, T. W. Frequency comb spectroscopy. *Nat. Photon.* **13**, 146–157 (2019).
7. Bao, C. et al. Architecture for microcomb-based GHz-mid-infrared dual-comb spectroscopy. *Nat. Commun.* **12**, 6573 (2021).
8. Kippenberg, T. J., Holzwarth, R. & Diddams, S. A. Microresonator-based optical frequency combs. *Science* **332**, 555–559 (2011).
9. Chang, L., Liu, S. & Bowers, J. E. Integrated optical frequency comb technologies. *Nat. Photon.* **16**, 95–108 (2022).
10. Zhang, M. et al. Broadband electro-optic frequency comb generation in a lithium niobate microring resonator. *Nature* **568**, 373–377 (2019).
11. Shen, B. et al. Integrated turnkey soliton microcombs. *Nature* **582**, 365–369 (2020).
12. Siegman, A. E. *Lasers* (Univ. Science Books, 1986).
13. Okawachi, Y. et al. Octave-spanning frequency comb generation in a silicon nitride chip. *Opt. Lett.* **36**, 3398–3400 (2011).
14. Brasch, V. et al. Photonic chip-based optical frequency comb using soliton cherenkov radiation. *Science* **351**, 357–360 (2016).
15. Jung, H., Xiong, C., Fong, K. Y., Zhang, X. & Tang, H. X. Optical frequency comb generation from aluminum nitride microring resonator. *Opt. Lett.* **38**, 2810–2813 (2013).
16. Guidry, M. A., Lukin, D. M., Yang, K. Y., Trivedi, R. & Vučković, J. Quantum optics of soliton microcombs. *Nat. Photon.* **16**, 52–58 (2021).
17. Wang, C. et al. Monolithic lithium niobate photonic circuits for kerr frequency comb generation and modulation. *Nat. Commun.* **10**, 978 (2019).
18. Hu, Y. et al. High-efficiency and broadband on-chip electro-optic frequency comb generators. *Nat. Photon.* **16**, 679–685 (2022).
19. Yu, M. et al. Integrated femtosecond pulse generator on thin-film lithium niobate. *Nature* **612**, 252–258 (2022).
20. Diddams, S. A., Ma, L.-S., Ye, J. & Hall, J. L. Broadband optical frequency comb generation with a phase-modulated parametric oscillator. *Opt. Lett.* **24**, 1747–1749 (1999).
21. Esteban-Martin, A., Samanta, G. K., Devi, K., Kumar, S. C. & Ebrahim-Zadeh, M. Frequency-modulation-mode-locked optical parametric oscillator. *Opt. Lett.* **37**, 115–117 (2012).
22. Okawachi, Y. et al. Competition between Raman and Kerr effects in microresonator comb generation. *Opt. Lett.* **42**, 2786–2789 (2017).
23. Boes, A. et al. Lithium niobate photonics: Unlocking the electromagnetic spectrum. *Science* **379**, eabj4396 (2023).
24. Wang, C. et al. Integrated lithium niobate electro-optic modulators operating at CMOS-compatible voltages. *Nature* **562**, 101–104 (2018).
25. Li, M. et al. Lithium niobate photonic-crystal electro-optic modulator. *Nat. Commun.* **11**, 4123 (2020).
26. Jankowski, M. et al. Ultrabroadband nonlinear optics in nanophotonic periodically poled lithium niobate waveguides. *Optica* **7**, 40–46 (2020).
27. Hwang, A. Y. et al. Mid-infrared spectroscopy with a broadly tunable thin-film lithium niobate optical parametric oscillator. *Optica* **10**, 1535–1542 (2023).
28. Park, T. et al. High-efficiency second harmonic generation of blue light on thin-film lithium niobate. *Opt. Lett.* **47**, 2706–2709 (2022).
29. Kashiwazaki, T. et al. Continuous-wave 6-dB-squeezed light with 2.5-THz-bandwidth from single-mode PPLN waveguide. *APL Photon.* **5**, 036104 (2020).
30. Nehra, R. et al. Few-cycle vacuum squeezing in nanophotonics. *Science* **377**, 1333–1337 (2022).
31. Lu, J. et al. Ultralow-threshold thin-film lithium niobate optical parametric oscillator. *Optica* **8**, 539–544 (2021).
32. McKenna, T. P. et al. Ultra-low-power second-order nonlinear optics on a chip. *Nat. Commun.* **13**, 4532 (2022).
33. Ledezma, L. et al. Octave-spanning tunable infrared parametric oscillators in nanophotonics. *Sci. Adv.* **9**, eadff0711 (2023).
34. Li, M. et al. Integrated Pockels laser. *Nat. Commun.* **13**, 5344 (2022).
35. Stokowski, H. S. et al. Integrated quantum optical phase sensor in thin film lithium niobate. *Nat. Commun.* **14**, 3355 (2023).
36. Luke, K. et al. Wafer-scale low-loss lithium niobate photonic integrated circuits. *Opt. Exp.* **28**, 24452–24458 (2020).
37. Li, Z. et al. High density lithium niobate photonic integrated circuits. *Nat. Commun.* **14**, 4856 (2023).
38. Xue, X., Zheng, X. & Zhou, B. Super-efficient temporal solitons in mutually coupled optical cavities. *Nat. Photon.* **13**, 616–622 (2019).
39. Helgason, Ó. B. et al. Power-efficient soliton microcombs. Preprint at <https://arxiv.org/abs/2202.09410> (2022).
40. Li, J. et al. Efficiency of pulse pumped soliton microcombs. *Optica* **9**, 231–239 (2022).
41. Harris, S. E. & Targ, R. FM oscillation of the He-Ne laser. *Appl. Phys. Lett.* **5**, 202–204 (1964).
42. Kuizenga, D. & Siegman, A. FM-laser operation of the Nd:YAG laser. *IEEE J. Quantum Electron.* **6**, 673–677 (1970).
43. Eckardt, R. C., Nabors, C. D., Kozlovsky, W. J. & Byer, R. L. Optical parametric oscillator frequency tuning and control. *J. Opt. Soc. Am. B* **8**, 646–667 (1991).
44. Ling, J. et al. Self-injection locked frequency conversion laser. *Laser Photon. Rev.* **17**, 2200663 (2023).
45. Op de Beeck, C. et al. III-V-on-lithium niobate amplifiers and lasers. *Optica* **8**, 1288–1289 (2021).
46. Del'Haye, P. et al. Phase-coherent microwave-to-optical link with a self-referenced microcomb. *Nat. Photon.* **10**, 516–520 (2016).
47. Mishra, J. et al. Ultra-broadband mid-infrared generation in dispersion-engineered thin-film lithium niobate. *Opt. Exp.* **30**, 32752–32760 (2022).
48. Celik, O. T. et al. High-bandwidth CMOS-voltage-level electro-optic modulation of 780 nm light in thin-film lithium niobate. *Optics Express* **30**, 23177–23186 (2022).
49. Sordillo, L. A. & Sordillo, P. P. (eds) *Short-Wavelength Infrared Windows for Biomedical Applications* (SPIE Press, 2022).
50. Willer, U., Saraji, M., Khorsandi, A., Geiser, P. & Schade, W. Near- and mid-infrared laser monitoring of industrial processes, environment and security applications. *Opt. Lasers Eng.* **44**, 699–710 (2006).
51. Goldenstein, C. S., Spearin, R., Jeffries, J. B. & Hanson, R. K. Infrared laser-absorption sensing for combustion gases. *Prog. Energy Combust. Sci.* **60**, 132–176 (2017).
52. Martin, A. et al. Photonic integrated circuit-based FMCW coherent LiDAR. *J. Lightwave Technol.* **36**, 4640–4645 (2018).

**Publisher's note** Springer Nature remains neutral with regard to jurisdictional claims in published maps and institutional affiliations.

Springer Nature or its licensor (e.g. a society or other partner) holds exclusive rights to this article under a publishing agreement with the author(s) or other rightsholder(s); author self-archiving of the accepted manuscript version of this article is solely governed by the terms of such publishing agreement and applicable law.

© The Author(s), under exclusive licence to Springer Nature Limited 2024

## Methods

### Device design and fabrication

We design our waveguide geometry to maximize the normalized efficiency and interaction rate. Extended Data Fig. 1a shows a schematic of the periodically poled, X-cut LN waveguide. We chose the ridge height  $h = 300$  nm, slab thickness  $s = 200$  nm, top width  $w = 1.2 \mu\text{m}$  and  $\text{SiO}_2$  cladding thickness  $c = 700$  nm. We find the guided modes by numerically solving Maxwell's equations with a finite-element solver (COMSOL). Extended Data Fig. 1a shows the  $E_x$  field distribution for a mode at 1,550 nm. Extended Data Fig. 1b presents the bands of the effective index as a function of wavelength in our waveguide geometry. The blue line highlights the fundamental transverse electric mode we use in our nonlinear waveguide and EO modulator. The difference between the effective index at the fundamental and second-harmonic frequency  $\Delta n_{\text{eff}}$  results in phase mismatch that we compensate for with periodic poling with a period of around  $\Lambda = \lambda_{\text{SH}}/\Delta n_{\text{eff}} = 3.7 \mu\text{m}$ . The LN waveguide forms a racetrack resonator with an intracavity directional coupler designed to close the resonator for the fundamental harmonic but ensures that the second-harmonic pump does not circulate. We call this design a 'snail resonator'. All the waveguide bends are defined by Euler curves to minimize light scattering between straight and bent waveguide sections.

We periodically pole the thin-film LN before the waveguide fabrication by patterning chromium finger electrodes on top of an insulating  $\text{SiO}_2$  layer. Extended Data Fig. 1c shows a scanning electron microscope (SEM) micrograph of a poling electrode. Next, we apply short pulses on the order of 1 kV to invert the ferroelectric domains and then verify the poling with a second-harmonic microscope. Extended Data Fig. 1d shows a periodically poled film. In the second-harmonic microscope picture, the black areas on the sides of the image correspond to the metal electrodes. The oblong shapes stretching between fingers correspond to the inverted LN domains. White regions at the centre of the inverted domains correspond to the poling that extends throughout the full depth of the thin-film LN. We pattern the critical waveguides within the fully poled film regions by aligning the electron-beam lithography mask in the waveguide patterning step.

Extended Data Fig. 2 presents the fabrication process flow. We start with a thin-film LN on an insulator chip (Extended Data Fig. 2a). We use 500 nm LN film bonded to around 2  $\mu\text{m}$  of  $\text{SiO}_2$  on a silicon handle wafer (from NanoLN). Then, we deposit about 100 nm of silicon dioxide using plasma-enhanced chemical vapour deposition (PlasmaTherm Shuttlelock PECVD System), which serves as a protective layer and prevents leakage current during poling. We pattern 100 nm thick chromium electrodes (evaporated with Kurt J. Lesker e-beam evaporator) on top of the insulating layer through electron-beam lithography (JEOL 6300-FS, 100-kV) and lift-off process and apply short voltage pulses to invert the LN domains (Extended Data Fig. 2b). Next, we remove the chromium and  $\text{SiO}_2$  layers with chromium etchant and buffered oxide etchant to obtain a poled thin-film LN chip (Extended Data Fig. 2c). We follow with waveguide patterning using JEOL 6300-FS electron-beam lithography and hydrogen silsesquioxane mask (FOx-16). We transfer the mask to the LN material using dry etching with an argon ion mill (Extended Data Fig. 2d). After the waveguide fabrication, we pattern another lift-off mask with electron-beam lithography to pattern electrodes for our EO modulators (Extended Data Fig. 2e). We use 200 nm of gold with a 15-nm chromium adhesion layer evaporated with the e-beam evaporator. We clad the entire chip with a layer of 700-nm thick  $\text{SiO}_2$  deposited with a high-density plasma chemical vapour deposition using PlasmaTherm Versaline HDP CVD System (Extended Data Fig. 2f) and open vias to access electrodes using inductively coupled plasma reactive ion etching (Extended Data Fig. 2g). We finish preparing the chip facets for light coupling by stealth dicing with a DISCO DFL7340 laser saw.

### Experimental setup

We characterize the FM-OPO and OPO response of our devices using the setup in Extended Data Fig. 3. We colour-code the paths intended to use with various signals: light orange corresponds to the fundamental-harmonic light (around 1,500–1,600 nm), the blue path corresponds to the second-harmonic (around 750–800 nm), and green corresponds to the RF signals. We drive our devices with a tunable C-band laser (Santec TSL-550, 1,480–1,630 nm) that we amplify with an erbium-doped fibre amplifier to around 1 W. We attenuate the optical power most of the time. We control the optical power to the chip with an MEMS variable optical attenuator (from OZ Optics) and calibrate the power using a 5% tap and a power meter (Newport 918D-IR-OD3R). The wavelength of the laser is controlled in a feedback loop using a wavelength meter (Bristol Instruments 621B-NIR). The light then passes through a fibre polarization controller and couples to the chip facet through a lensed fibre. We deliver RF signals to the chip through a ground–signal–ground probe (GGB Industries Picoprobe 40A). We use Keysight E8257D PSG Analog Signal Generator as an RF source and amplify it with a high-power amplifier (Mini-Circuits ZHL-5W-63-S+). We place a circulator before the chip to avoid any reflections into the source and terminate the reflected port after passing it through a 20-dB attenuator.

The generated light is split between two paths with a 1,000-nm short-pass dichroic mirror (Thorlabs DMSP1000). The two paths are connected to the InGaAs and Si avalanche photodiodes (Thorlabs APD410A and Thorlabs APD410) to detect the fundamental- and second-harmonic power, respectively. VOAs precede both avalanche photodiodes (APDs) to avoid saturation and increase the dynamic range of the measurements (HP 8156A and Thorlabs FW102C). Part of the fundamental-harmonic path splits into an optical spectrum analyser (Yokogawa AQ6370C) and a fast photodetector (New Focus 1554-B-50), the response of which is characterized by an RF spectrum analyser (Rohde & Schwarz FSW26).

### Intracavity coupler characterization

We characterize the performance of the intracavity coupler using a smaller racetrack resonator with a 2-mm straight section. Extended Data Fig. 4a shows the normalized transmission of the cavity (Extended Data Fig. 4b). The variation in intrinsic and extrinsic quality factors changes cavity-mode contrast across the wavelength range. This results in a transition from an undercoupled cavity at 1,500 nm to critically coupled at 1,550 nm and overcoupled at 1,580 nm. We confirm this by fitting the quality factors for all modes. For instance, in Fig. 4c, we find  $Q_i \approx 2.5 \times 10^6$  and  $Q_e \approx 0.8 \times 10^6$ . Extended Data Fig. 4d plots the quality factors against wavelength, highlighting a  $Q_i$  peak near 1,580 nm, corresponding to the maximum coupler transmission. We use the same coupler in the FM-OPO resonator, but we increase the straight section length to 10 mm, resulting in flattened  $Q_i$  wavelength dependence.

### Dispersion measurement

The second-order dispersion  $\zeta_2$  is an important parameter of the FM-OPO because it determines the comb span and tunability. To quantify it, we modify the measurement setup by adding another 5% tap connected to a fibre Mach–Zehnder interferometer (MZI) and a photodetector (Newport 1623 Nanosecond Photodetector) (Extended Data Fig. 5a). We collect the MZI transmission and the cavity transmission while scanning the pump laser and calibrate the wavelength by unwrapping the phase in the MZI transmission spectrum. This method enables us to measure cavity-mode location with precision of the order of single MHz. We measure the FM-OPO cavity spectrum using the feed-line waveguide and extract the local FSR (Extended Data Fig. 5b). The discontinuity near 1,540 nm corresponds to a mode crossing between the fundamental and second-order TE modes. The relative position of cavity modes is defined by  $\omega_n = \omega_0 + \zeta_1 \times n + \zeta_2/2 \times n^2$ . We fit the FSR with

# Article

respect to the mode number and extract the second-order dispersion parameter  $\zeta_2/2\pi \approx -11$  kHz, which agrees with the theoretical prediction based on the finite-element simulation.

## Nonlinear coupling rates

We calculate the EO and optical nonlinear coupling rates from the interaction energy density in the  $\chi^{(2)}$  process:

$$U_{\chi^{(2)}} = \frac{\epsilon_0}{3} \sum_{\alpha\beta\gamma} \chi_{\alpha\beta\gamma}^{(2)} E^\alpha E^\beta E^\gamma, \quad (4)$$

where  $E^\alpha$ ,  $E^\beta$  and  $E^\gamma$  correspond to the electric field components polarized in different directions.

We consider a three-wave mixing process between two optical modes and one RF mode to find the EO coupling  $M$ . We neglect the fast-rotating terms under the rotating wave approximation and see that

$$\begin{aligned} U_{\chi^{(2)}}^c &= 2\epsilon_0 \sum_{\alpha\beta\gamma} \chi_{\alpha\beta\gamma}^{(2)} (E_n^{\alpha*} E_{n+1}^\beta E_c^\gamma a_n^* a_{n+1} c + \text{c.c.}) \\ &= 2\epsilon_0 (\mathbf{E}_n^* \bar{\chi}^{(2)} : \mathbf{E}_{n+1} \mathbf{E}_c a_n^* a_{n+1} c + \text{c.c.}). \end{aligned} \quad (5)$$

Here, c.c. is a complex conjugate. We integrate this energy density to obtain the total interaction energy used to derive the equations of motion. We normalize the field  $\mathbf{E}_i$  so that the total energy of the mode  $a_i$  is  $\hbar\omega_i |a_i|^2$  by introducing normalization factors:

$$\begin{aligned} N_i &= \sqrt{\frac{\hbar\omega_i}{2}} \frac{1}{\sqrt{\int_V \epsilon_0 \mathbf{e}_i \bar{\epsilon}_{r,a} \mathbf{e}_i dV}} \\ &= \sqrt{\frac{\hbar\omega_i}{2\epsilon_0 L}} \frac{1}{\sqrt{\mathcal{A}_i}}. \end{aligned} \quad (6)$$

This normalization enables us to use the unitless field profiles  $\mathbf{e}_i$  that satisfy  $\mathbf{E}_i = N_i \mathbf{e}_i$ . We also introduce the effective mode area for each mode as  $\mathcal{A}_i = \int \mathbf{e}_i \bar{\epsilon}_{r,a} \mathbf{e}_i dA$ . To find the energy, we integrate equation (5) and introduce a factor  $\lambda_{RF}$  that describes the fraction of the total racetrack resonator length  $L$  experiencing modulation. The EO coupling rate per volt is

$$M_0 = M/V = \sqrt{\lambda_{RF} \tilde{C}} \sqrt{\frac{2\omega_n \omega_{n+1}}{\epsilon_0}} \frac{\mathcal{O}_{EO}}{\sqrt{\mathcal{A}_n \mathcal{A}_{n+1} \mathcal{A}_c}} \quad (7)$$

where  $\tilde{C}$  is the capacitance of the electrode per unit length,  $\epsilon_n$  is the permittivity at frequency  $\omega_n$  and  $\mathcal{O}_{EO}$  is the mode overlap integral over the waveguide cross-section area.

$$\mathcal{O}_{EO} = \int_A \mathbf{e}_n^* \bar{\chi}^{(2)} : \mathbf{e}_{n+1} \mathbf{e}_c dA, \quad (8)$$

where  $\bar{\chi}^{(2)}$  is the second order susceptibility tensor. We use a finite-element mode solver (COMSOL) to calculate the coupling rate per volt of our device at around 130 MHz V<sup>-1</sup>.

We calculate the optical nonlinear coupling rate  $g$  by considering three optical modes  $m$ ,  $n$  and  $k$  in equation (4). Applying the rotating wave approximation and normalization defined by equation (6) yields

$$g = \frac{\lambda_{pp}}{\sqrt{2\pi}} \sqrt{\frac{\hbar\omega_m \omega_n \omega_k}{\epsilon_0 L}} \frac{\mathcal{O}_{opt}}{\sqrt{\mathcal{A}_m \mathcal{A}_n \mathcal{A}_k}}, \quad (9)$$

where  $\lambda_{pp}$  describes the fraction of the length of the resonator that is periodically poled and  $\mathcal{O}_{opt}$  represents the mode overlap integral over the waveguide cross-section area:

$$\mathcal{O}_{opt} = \int_A \mathbf{e}_k^* \bar{\chi}^{(2)} : \mathbf{e}_m \mathbf{e}_n dA. \quad (10)$$

We evaluate this expression numerically using COMSOL to find  $g/2\pi \approx 67$  kHz.

## Optical nonlinearity characterization

We analyse the nonlinear performance of our periodically poled LN waveguides using a second-harmonic generation measurement in a waveguide from the same poled area as the FM-OPO waveguides. The setup is shown in Extended Data Fig. 6a, with a similar input to our general setup. Two APDs collect output as in FM-OPO measurements. Extended Data Fig. 6b shows a measured second-harmonic generation transfer function from a C-band laser sweep at about 200  $\mu$ W power on a 7-mm waveguide. Minor distortions result from waveguide non-uniformity. Extended Data Fig. 6c presents peak second-harmonic power measured as a function of on-chip pump power, with an inset showing a bright second-harmonic spot at the end of the waveguide. We used a quadratic fit to derive the normalized efficiency  $\eta$ :

$$P_{SH} = \eta P_{FH}^2 L^2, \quad (11)$$

where  $L$  is the length of the periodically poled LN waveguide,  $P_{SH}$  and  $P_{FH}$  correspond to the power of the second harmonic and fundamental harmonic, respectively. We extract a normalized efficiency of around 1,500% W<sup>-1</sup> cm<sup>-2</sup>, corresponding to the interaction rate around  $g/2\pi \approx 67$  kHz, which agrees with our theory. The measured FM-OPO operates away from the perfect quasi-phase matching,  $\Delta k \neq 0$ , which reduces the interaction rate to around 12 kHz.

## EO characterization

To evaluate the FM-OPO EO performance, we drive the cavity with RF and measure the transmission spectra using setup from Extended Data Fig. 7a. Without RF, the cavity shows a Lorentzian lineshape (Extended Data Fig. 7b) with an intrinsic quality factor of about  $Q_i \approx 1 \times 10^6$ . With RF modulation, the shape distorts. We model this by adding a fundamental-harmonic drive for the  $n = 0$  mode to the FM-OPO cavity coupled-mode equation (2):

$$\begin{aligned} \dot{a}_n &= \left( i \left( \Delta - \frac{n^2 \zeta_2}{2} \right) - \frac{\kappa_{a,n}}{2} \right) a_n \\ &\quad - iM(a_{n-1} + a_{n+1}) + i \sqrt{\frac{\kappa_a^{(e)} P_{FH}}{\hbar\omega_a}} \delta_{n,0}. \end{aligned} \quad (12)$$

Here,  $\Delta$  is the laser detuning and  $\delta_{n,0}$  is the Kronecker delta. We model the EO-modulated cavity response by solving this system of equations for 50 modes in steady state:

$$0 = M A + B, \quad (13)$$

where  $M$  is the matrix including pump detuning, loss rates of the cavity modes, and EO coupling,  $B(n = 0) = i \sqrt{(\kappa_a^{(e)} P_{FH}) / (\hbar\omega_a)}$  and  $B(n \neq 0) = 0$ . We find  $A = -M^{-1}B$ . The total output power of the cavity consists of the laser pump interfering with the intracavity field and a sum of all the generated sidebands:

$$|a_{out}|^2 = |a_{in} - i \sqrt{\kappa_0^{(e)}} a_0|^2 + \sum_{n \neq 0} \kappa_n^{(e)} |a_n|^2. \quad (14)$$

We numerically evaluate the model to fit the transmission shapes for various peak voltages. In Extended Data Fig. 7b, the orange points represent data from the cavity modulated at about  $V_p \approx 4.5$  V, with the red line as the fit. We fix the quality factors from the unmodulated line for modulated shapes and derive only the EO coupling  $M$  from each fit. In Extended Data Fig. 7c, we plot EO coupling  $M/2\pi$  against peak voltage, fitting a line to determine the dependence of EO coupling on voltage. The measured value,  $M_0/2\pi \approx 60$  MHz V<sup>-1</sup>, is close to the predicted 130 MHz V<sup>-1</sup>.

## RF and optical spectra of the FM-OPO

We examine the FM-OPO combs we produce using a high-speed photodetector and an RF spectrum analyser. A single FM-OPO, as defined by equations (derived in SI),

$$a_i(t) = A_i e^{-i\omega_i t} e^{i\Gamma \sin(\Omega t)} e^{i\omega_p t/2} \quad (15)$$

$$a_s(t) = A_s e^{-i\omega_s t} e^{-i\Gamma \sin(\Omega t)} e^{i\omega_p t/2}, \quad (16)$$

should not create any detectable RF tones when evaluated with a fast photodetector because a pure phase or frequency modulation will not be detected on a photodiode measuring intensity. However, we observe peaks in the RF spectra for the FM-OPOs shown in Fig. 4a that are spaced by  $\Omega$ . These are shown in Extended Data Fig. 8a, and we provide a closer look at the first sidebands in Extended Data Fig. 8b. The extra features observed experimentally probably result from the multi-cluster character of the comb at a high-power RF drive that our simple model does not capture.

We find that even a minor dependence of the external coupler transmission of the cavity on wavelength can lead to a noticeable conversion from frequency modulation to intensity modulation. To confirm this, we estimate the expected result of a high-speed photodiode measurement of signal and idler combs produced following equations (15) and (16), under the influence of a wavelength-dependent coupler. We determine the external coupling as a function of frequency for our cavity from the same measurement we used for dispersion characterization. The average change in the external coupling across the 1,500–1,600 nm measurement bandwidth is approximately  $\partial k_a^{(e)} / \partial \omega \approx -5 \times 10^{-6}$ . The calculated RF spectra (Extended Data Fig. 8c) qualitatively match our experimental observations, with discrepancies occurring at higher EO modulation rates where the single FM-OPO approximation is no longer applicable. For each RF spectrum, we also present the full optical spectra (including signal and idler) in Extended Data Fig. 8d.

We plot the spectrum with the largest observed coverage, measured at around 1.2 W of RF power in Extended Data Fig. 8e. Note that for a particular pump wavelength, there are several possible modes of oscillation corresponding to the coupling between different mode pairs  $(-n_{osc}, n_{osc}), (-n_{osc} - 1, n_{osc}), (-n_{osc} - 1, n_{osc} - 1)$  and so on. For the non-modulated OPO operation at the power levels we experimentally characterized, we observe only one oscillating mode at a fixed pump wavelength (that is,  $(-n_{osc}, n_{osc})$ ), which we attribute to optimal phase matching. Adjusting the pump results in switching between different mode pairs with a periodicity of 1/2 FSR. However, in the presence of sufficiently strong modulation, clusters of modes arise in the FM-OPO spectrum corresponding to these secondary mode pairs being excited.

## FM-OPO tuning with laser and RF detuning

We experimentally analyse the behaviour of FM-OPO comb properties with respect to the RF drive parameters. First, we step the pump laser across one FSR of the cavity (Extended Data Fig. 9a) and record the optical spectrum analyser spectra for various EO coupling rates (Extended Data Fig. 9b–d). We can calibrate the pump wavelength, as shown in Extended Data Fig. 9a with respect to the cavity modes by looking at the slight leakage of the original FH pump visible as a faint line at around 1,554 nm signal wavelength in all the colourmaps. In this study, we operate in a non-degenerate regime and observe a pure OPO in Extended Data Fig. 9b. Next, by switching on a moderate RF modulation, we achieve  $M/2\pi \approx 100$  MHz in Extended Data Fig. 9c and observe comb formation and higher-order FM-OPO comb development. Finally, at high modulation of around  $M/2\pi \approx 510$  MHz, we observe that the combs originating from different OPO modes  $(-n_{osc}, n_{osc}), (-n_{osc} + 1, n_{osc})$  and  $(-n_{osc} + 1, n_{osc} + 1)$  start to merge. We note that the areas with suppressed FM-OPO intensity result from the waveguide mode crossings between

the fundamental TE mode and higher-order modes that effectively reduce the quality factors in that region. Next, we analyse the FM-OPO response to the RF detuning  $\delta$ , shown schematically in Extended Data Fig. 9e. We measure this by pumping the device at around 1545 nm and using  $M/2\pi \approx 510$  MHz. For most measurements, we fix the detuning to  $\delta = 0$  so that the RF frequency is in resonance with the cavity FSR near degeneracy  $\Omega = \zeta_1$  to maximize the comb span and output optical power. If the RF drive is detuned, we observe comb shrinking, as shown in Extended Data Fig. 9f, and the total output power decreases, as shown in Extended Data Fig. 9g.

## Uncertainty analysis

The measurement error of the comb count in Fig. 4b is given by the standard deviation of 51 measurements (41 measurements for the highest RF power). The shaded region corresponds to the coupled-mode-equation simulation, from which we extract the half-widths of the simulated combs. We assume uncertainty of  $\pm 1$  mode on each side of the signal and idler combs. We calculate the uncertainty of the measured depletion of the second-harmonic pump (Fig. 4c) and the measured OPO signal (Fig. 4d) based on the standard deviation of the second-harmonic and fundamental signals over the measurement time.

We measure the average intrinsic and total quality factors of the FM-OPO resonator by averaging the results of Lorentzian fits over around 20 nm of the spectrum, in which we observe the comb formation. The standard deviation gives their uncertainties. We infer the uncertainty of  $\kappa_b$  based on the precision of our estimation of the group index ( $10^{-3}$ , based on the finite-element solver). We calculate the cavity escape efficiency uncertainty based on the errors of the average quality factors. The uncertainties of the cavity FSR, cavity dispersion, peak waveguide nonlinear efficiency and electro-optically induced mode-coupling rate correspond to the standard errors of the fit parameters extracted from the least-square fitting. Uncertainties of the nonlinear interaction rate and the second-harmonic power threshold of the OPO are calculated based on the standard errors of a nonlinear fit. We calculate the internal and total OPO efficiency errors based on the cavity escape efficiency and second-harmonic depletion uncertainties.

**Acknowledgements** This work was supported by the US government through the Defense Advanced Research Projects Agency Young Faculty Award and Director's Fellowship (YFA, grant no. D19AP00040), the LUMOS programme (grant no. HR0011-20-2-0046), the US Department of Energy (grant no. DE-AC02-76SF00515) and the Q-NEXT NQI Center; the US Air Force Office of Scientific Research provided an MURI grant (grant no. FA9550-17-1-0002, received by A.H.S.-N.). We thank NTT Research for their financial and technical support. H.S.S. acknowledges support from the Urbanek Family Fellowship, and V.A. was partially supported by the Stanford Q-Farm Bloch Fellowship Program and the Max Planck Society Sabbatical Fellowship Award. This work was also performed at the Stanford Nano Shared Facilities (SNSF), supported by the National Science Foundation under award ECCS-2026822. We also acknowledge the Q-NEXT DOE NQI Center and the David and Lucile Packard Fellowship for their support. D.J.D. and A.Y.H. acknowledge support from the NSF GRFP (grant no. DGE-1656518). H.S.S. and V.A. thank K. Multani and C. Sarabalis for their discussions and technical support. A.H.S.-N. thanks J. M. Kahn and S. E. Harris for their discussions.

**Author contributions** A.H.S.-N. and H.S.S. conceived the device and H.S.S. designed the photonic integrated circuit. H.S.S., C.L., M.J. and T.P.M. developed the essential components of the photonic circuit. H.S.S., T.P. and A.Y.H. fabricated the device. H.S.S., V.A. and O.T.C. developed the fabrication process. M.M.F. and A.H.S.-N. provided experimental and theoretical support. H.S.S., T.P. and D.J.D. performed the experiments. H.S.S., A.Y.H., T.P. and D.J.D. analysed the data. H.S.S. and A.H.S.-N. wrote the paper. H.S.S., V.A. and A.H.S.-N. developed the experiment. H.S.S., D.J.D. and A.H.S.-N. developed the numerical and analytical models. A.H.S.-N. supervised all efforts.

**Competing interests** A.H.S.-N., H.S.S. and A.Y.H. are inventors of a patent application that covers the concept and implementation of the frequency-modulated optical parametric oscillator and its applications. The other authors declare no competing interests.

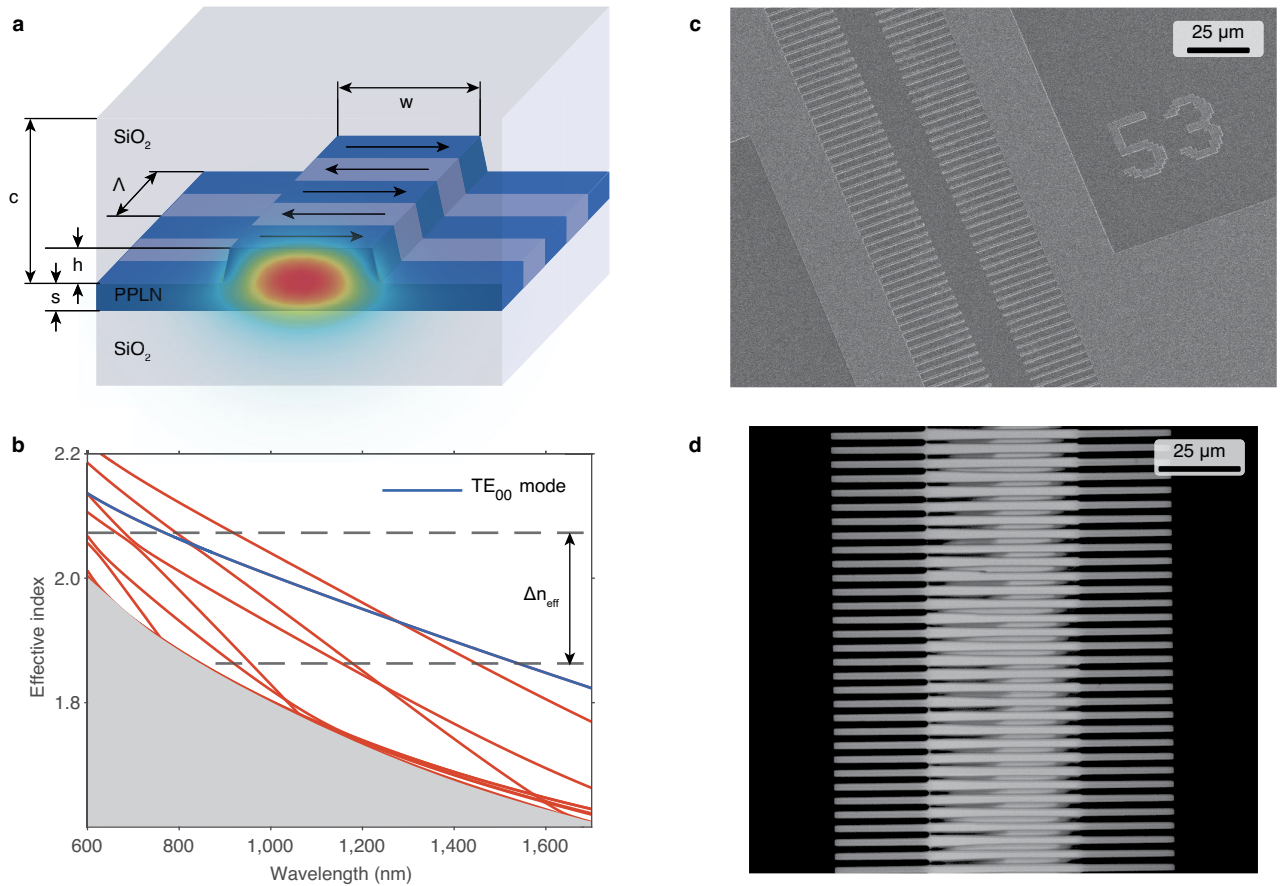
## Additional information

**Supplementary information** The online version contains supplementary material available at <https://doi.org/10.1038/s41586-024-07071-2>.

**Correspondence and requests for materials** should be addressed to Amir H. Safavi-Naeini.

**Peer review information** *Nature* thanks Laura Sinclair and the other, anonymous, reviewer(s) for their contribution to the peer review of this work. Peer reviewer reports are available.

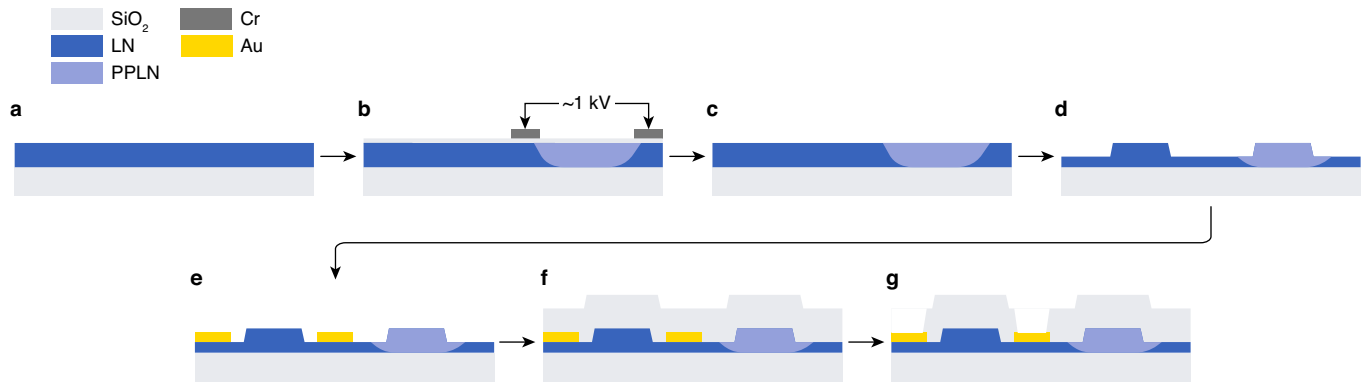
**Reprints and permissions information** is available at <http://www.nature.com/reprints>.



#### Extended Data Fig. 1 | Periodically poled lithium niobate waveguide design.

**a**, Schematic of a periodically poled lithium niobate waveguide, waveguide dimensions are: ridge height  $h = 300$  nm, slab height  $s = 200$  nm, width  $w = 1200$  nm, cladding thickness  $c = 700$  nm, poling period  $\Lambda = 3.7 \mu\text{m}$ . Thin-film lithium niobate is bonded to a  $2 \mu\text{m}$  thick silicon dioxide layer and clad with a PECVD layer of  $\text{SiO}_2$ . An eigenmode solution at 1550 nm is overlaid with the waveguide schematic. **b**, Effective index bands for various waveguide modes in our waveguide geometry. The blue line highlights the fundamental  $\text{TE}$  mode.

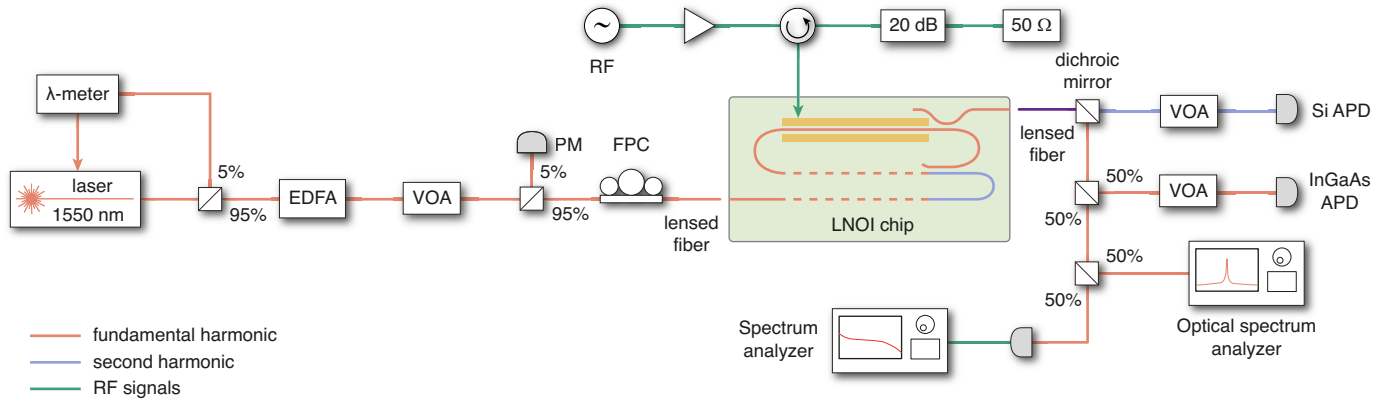
We compensate for the effective index mismatch  $\Delta n_{\text{eff}}$  between the fundamental and second harmonic with periodic poling of the film. **c**, SEM micrograph of a chromium electrode patterned on a thin-film-LN chip for poling. **d**, Second harmonic microscope picture of periodically poled thin-film LN. Black areas on the left and right correspond to Cr electrodes. Oblong, grayscale shapes between the finger electrodes are inverted crystal domains. White areas of the inverted domains correspond to the full-depth poling of the film.



**Extended Data Fig. 2 | Fabrication process of the photonic integrated circuit.** **a**, We start our fabrication process with a thin-film of lithium niobate on insulator. **b**, Next, we deposit a 100 nm protective layer of  $\text{SiO}_2$ , pattern Cr electrodes, and pole the LN by applying high voltage pulses. **c-d**, We remove

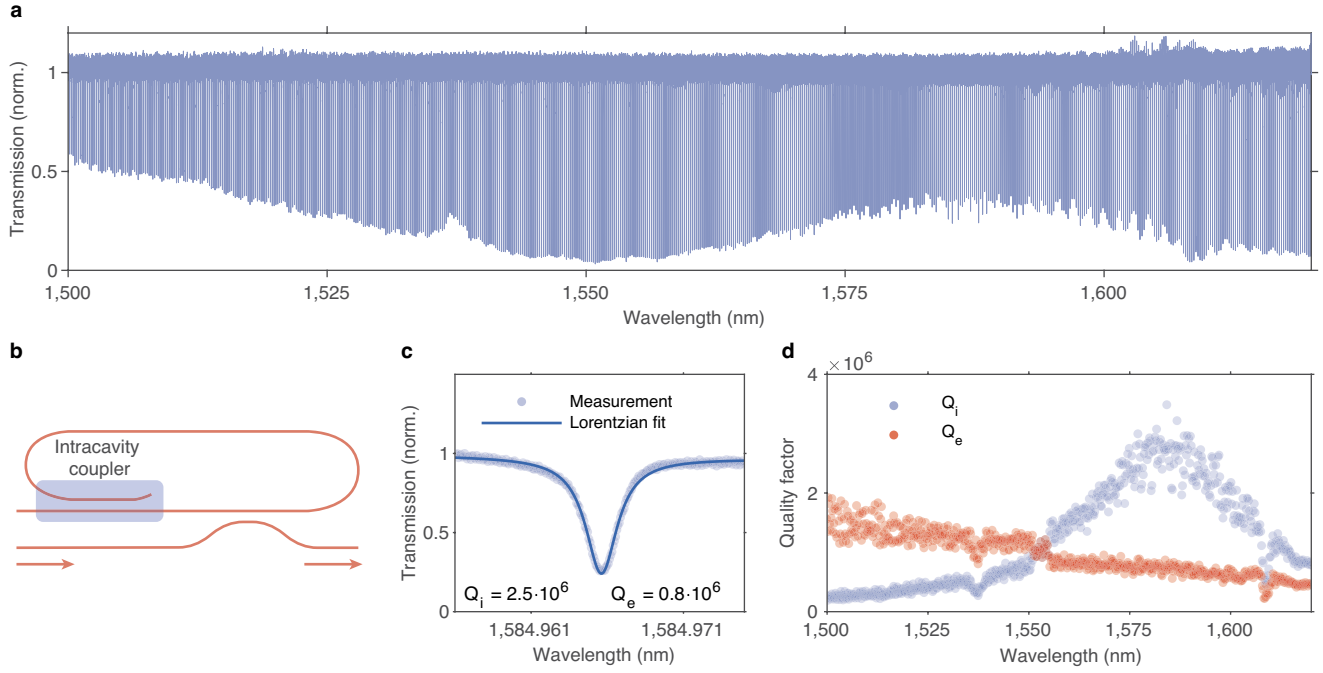
the  $\text{SiO}_2$  and Cr afterward and etch waveguides into the LN film through argon ion-mill dry etching. **e-f**, After the waveguide fabrication, we pattern gold electrodes with the lift-off process and clad the entire structure with  $\text{SiO}_2$ . **g**, Finally, we pattern vias in the  $\text{SiO}_2$  layer to access the metal electrodes.

# Article



**Extended Data Fig. 3 | Experimental setup for the FM-OPO characterization.** We characterize our devices with a C-band tunable laser that we amplify with an erbium-doped fiber amplifier (EDFA), yielding up to 1 W of optical power. We control the power going to the chip with a variable optical attenuator (VOA) and calibrate that power by splitting around 5% of laser into a power meter (PM). We control the polarization with a fiber polarization controller (FPC) and inject the light into a cleaved chip facet with a lensed fiber. We drive the FM-OPO with

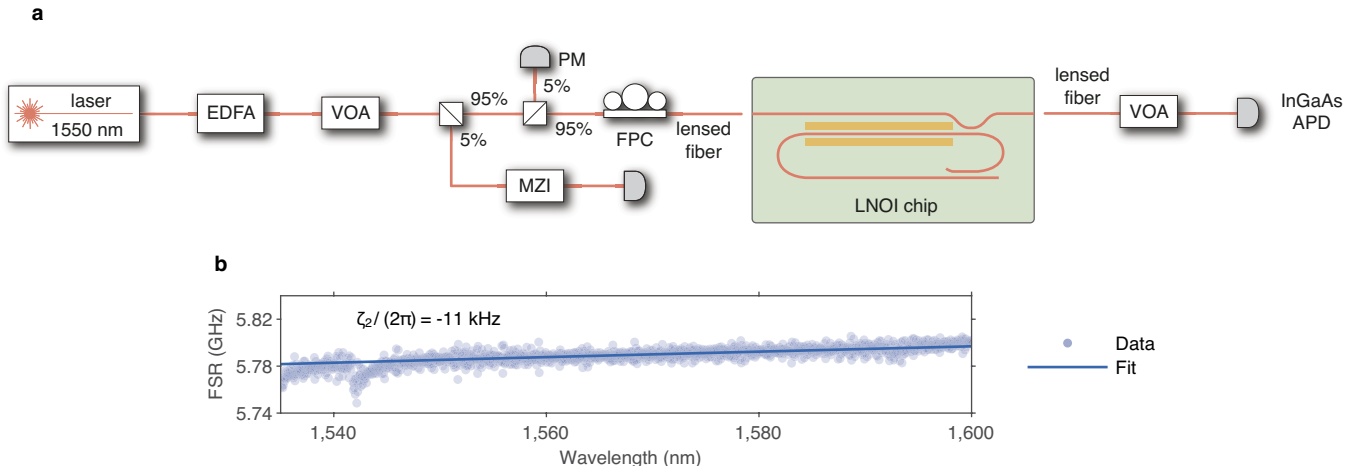
an RF source connected to an amplifier. We place a circulator before the chip to avoid reflections returning to the source. Any RF reflections are passed to termination through a 20 dB attenuator. We characterize the output of our devices by splitting the FH and SH light using a dichroic mirror. Both wavelengths are passed through VOAs for power control and measured with calibrated avalanche photodetectors (APDs). Finally, we split part of the FH light into an optical spectrum analyzer and a fast photodiode.



**Extended Data Fig. 4 | Intracavity coupler characterization.** **a**, Broadband transmission spectrum of a snail resonator with a straight section length of 2 mm. We observe mode contrast changing from under-coupled at 1500 nm to critically coupled at around 1550 nm to over-coupled at 1580 nm. **b**, Device measurement scheme, we probe a cavity with an internal coupler using an evanescent coupler feed waveguide. **c**, Zoom into a single cavity mode around 1585 nm, fitting a Lorentzian lineshape (solid blue line) reveals an intrinsic quality factor ( $Q_i$ ) of around 2.5 million and extrinsic quality factor ( $Q_e$ ) of

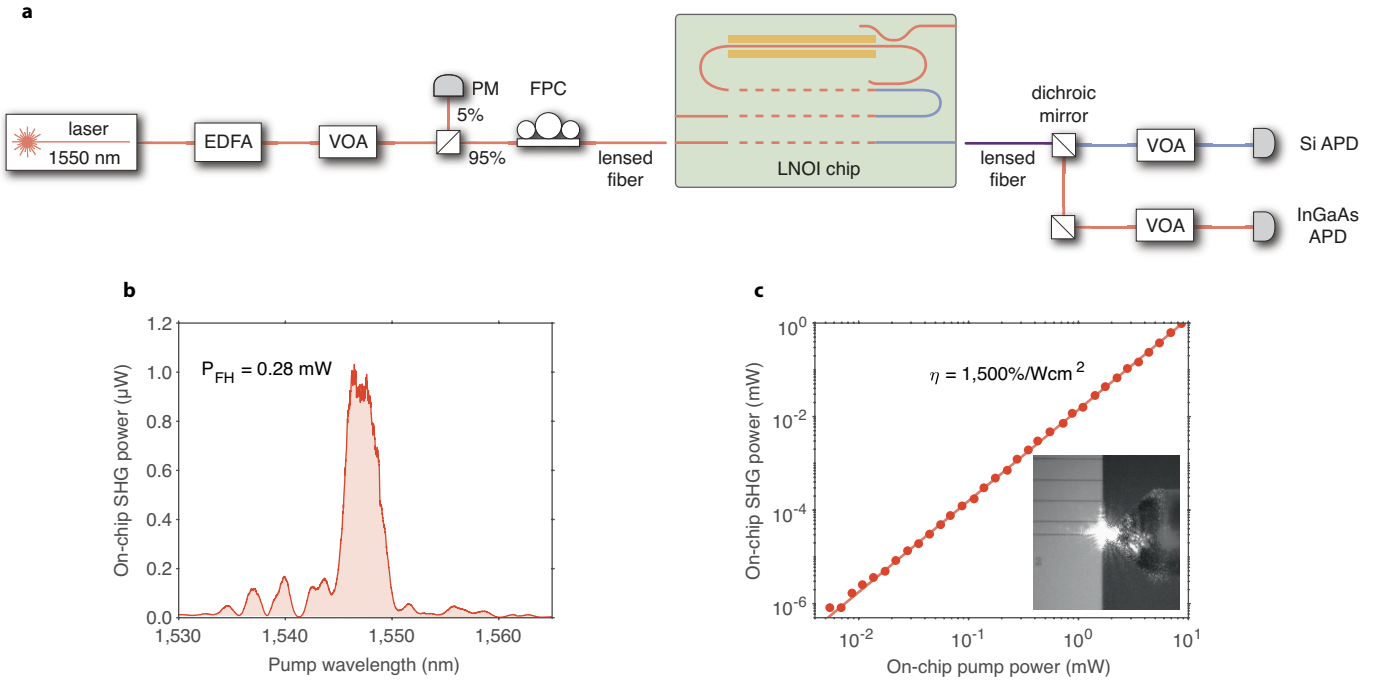
around 800,000. **d**, Intrinsic and extrinsic quality factors as a function of wavelength. We distinguish between the  $Q_i$  and  $Q_e$  by observing the wavelength dependence.  $Q_i$  peaks at around 1580 nm, where the intracavity coupler transmits all the light, thus forming a low-loss cavity.  $Q_e$  decreases with wavelength because modes become less confined and can couple stronger to neighboring waveguides. The region where  $Q_i \approx Q_e$  around 1552 nm is ambiguous; we report the same average number for both  $Q_i$  and  $Q_e$  there.

# Article



**Extended Data Fig. 5 | Second-order dispersion characterization of the optical cavity.** **a**, We characterize the second-order dispersion by probing the snail cavity with a broadband tunable C-band laser. We use a similar input setup to the one in Fig. 3 with an additional power splitter connected to a fiber MZI

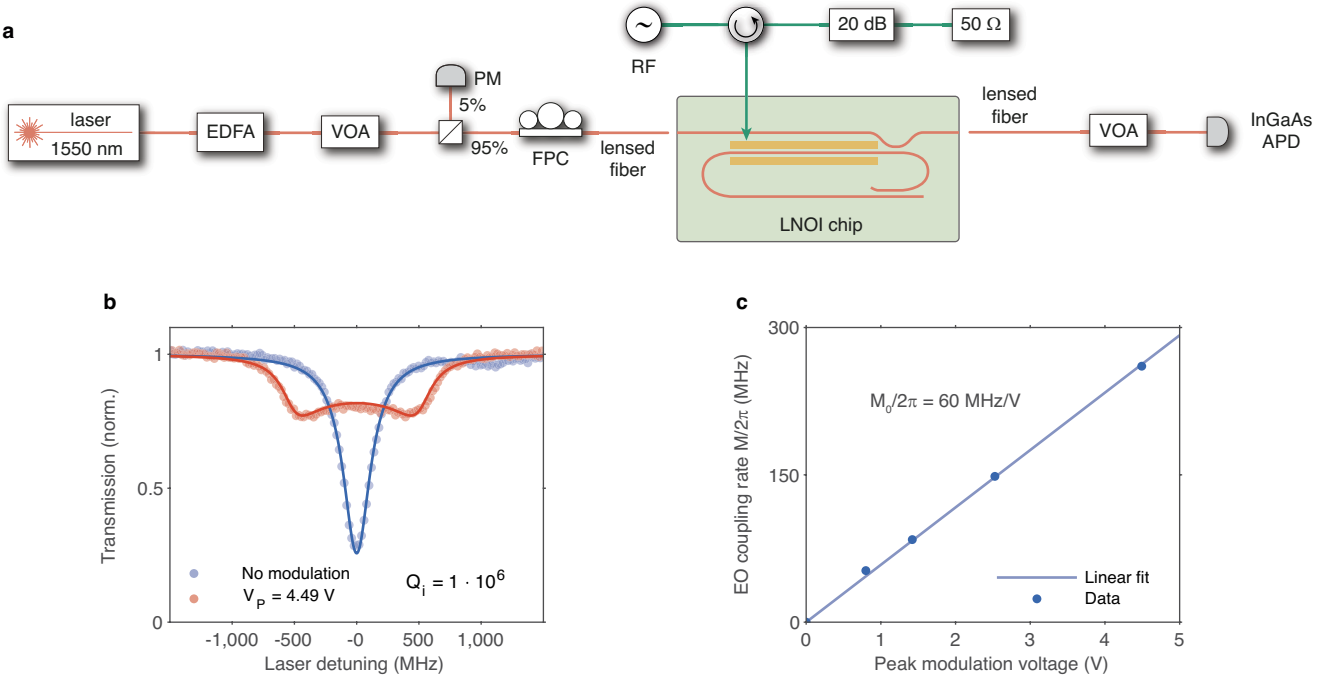
and detector, which serve as wavelength calibration. We collect the light with a setup with a VOA and an InGaAs APD. **b**, Measured free spectral range of the cavity as a function of wavelength. We find mode locations and fit a line to extract the second-order dispersion parameter of around  $\zeta_2/2\pi \approx -11$  kHz.



**Extended Data Fig. 6 | Characterization of the second-order optical nonlinearity.** **a**, Experimental setup for the second harmonic generation measurement. We use a similar input setup as in Fig. 3 and drive a periodically poled LN waveguide with a tunable C-band laser. We collect the output light into a fiber and split it with a dichroic mirror between two avalanche photodetectors (APDs) for FH and SH light characterization. **b**, Example

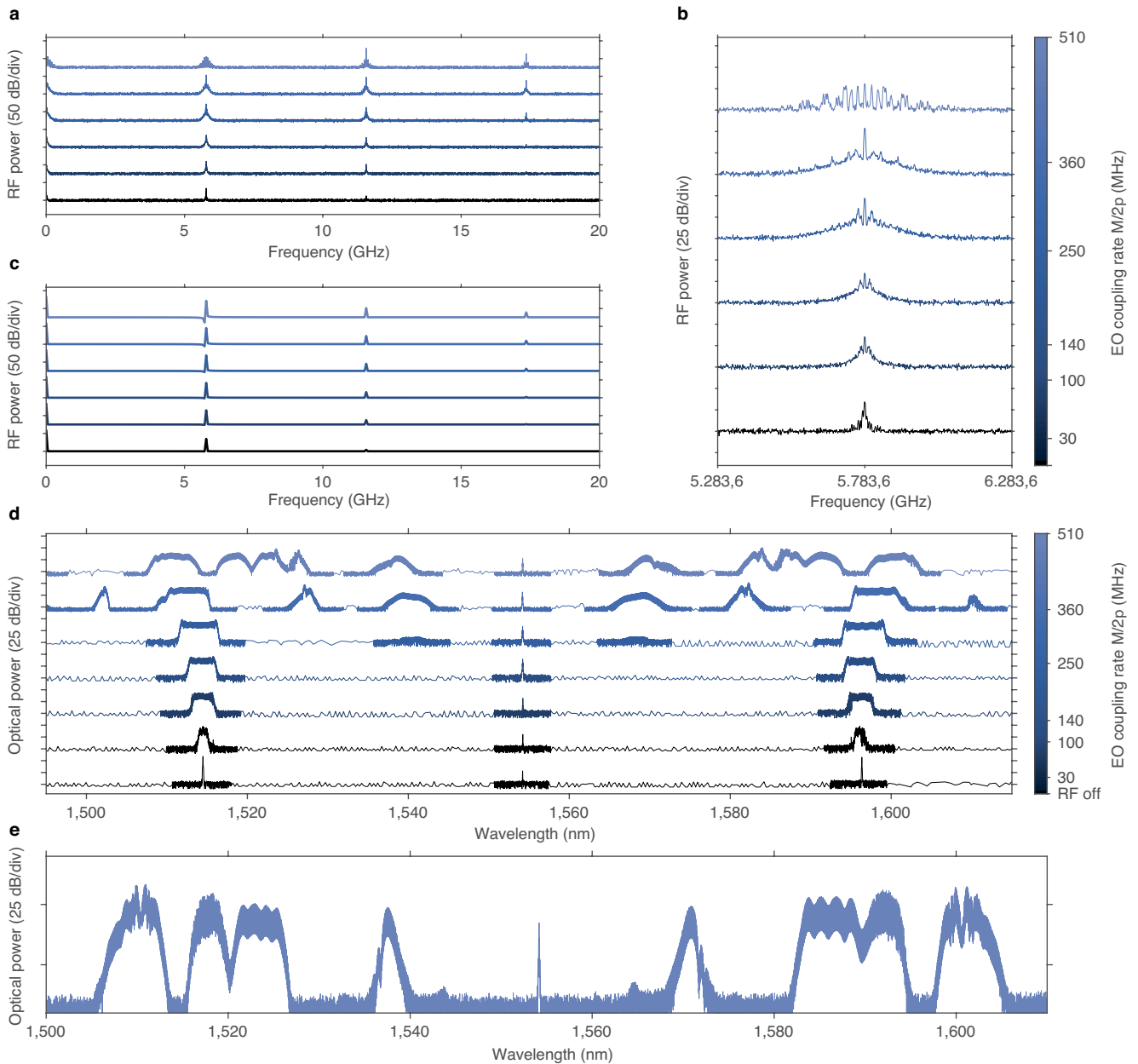
second harmonic generation transfer function measured at pump power of about  $P_{FH} \approx 200 \mu\text{W}$ . **c**, Measured second harmonic generation output power as a function of pump power. The quadratic fit yields a normalized efficiency of around  $\eta \approx 1,500 \%/\text{Wcm}^2$ . The inset shows a microscope picture of bright second harmonic light scattered at the output facet of the chip and collected into a lensed fiber.

# Article



**Extended Data Fig. 7 | Characterization of the electro-optic coupling to the snail resonator.** **a**, Experimental setup. We use a similar input path as in Fig. 3 and drive the device with a tunable C-band laser. In addition, we deliver RF signals from the source in the same way as in Fig. 3, except we do not use the microwave amplifier. We collect the light into an InGaAs avalanche photodiode (APD) through a variable optical attenuator (VOA). **b**, Normalized transmission

of a single cavity mode with (orange) and without RF drive (blue). Solid lines correspond to fitting the model. We drive the cavity with peak voltage of around  $V_p \approx 4.5 \text{ V}$  for the modulated dataset. **c**, Fitted electro-optic coupling  $M/2\pi$  as a function of peak modulation voltage. We extract  $M_0$  from curves like the ones in Fig. 7b and fit a line to find  $M_0/2\pi \approx 60 \text{ MHz/V}$ .

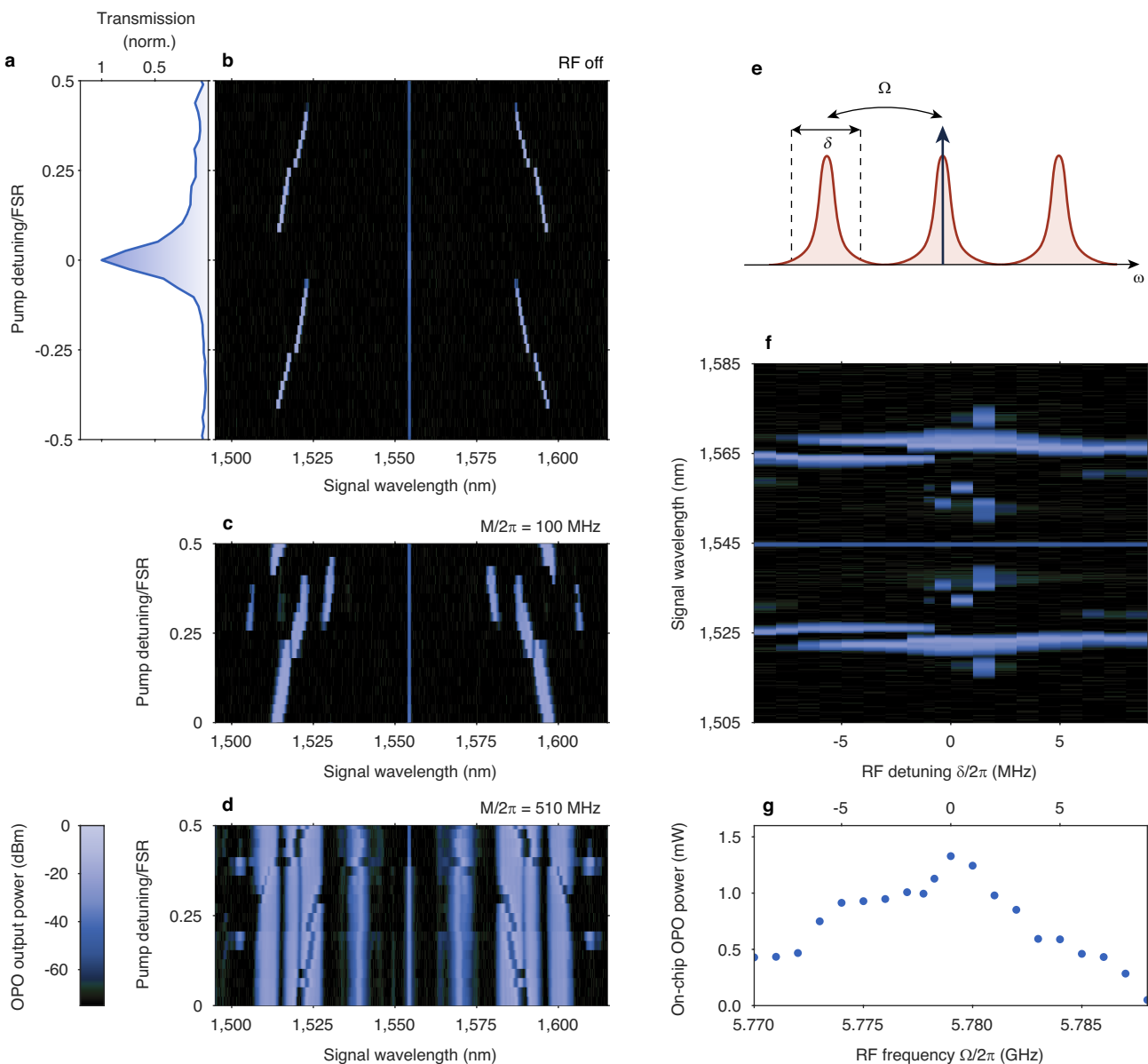


**Extended Data Fig. 8 | RF and optical spectra generated by the FM-OPO.**

**a**, Measured RF spectra generated by the FM-OPO as a function of the RF drive strength. **b**, Zoom-into the first sideband around 5.78 GHz shows additional features not predicted by our simple model, likely arising from the multi-cluster behavior at high RF power. **c**, Simulated RF spectra generated by an

FM-OPO coupled to a wavelength-dependent output coupler. **d**, Full optical spectrum analyzer spectra of the generated FM-OPO combs, partially plotted in Fig. 4a. **e**, Maximum spectral coverage of the FM-OPO, observed with around 1.2 W RF drive power.

# Article



**Extended Data Fig. 9 | FM-OPO tuning with laser and RF detuning.** **a**, Transmission of the leakage fundamental pump to the snail port of the resonator, corresponding to the OPO output in **b**. **b**, Pump-wavelength tuning of the OPO in a nondegenerate regime, the output wavelength tuning curves repeat with a period of  $1/2$  FSR with respect to the pump wavelength. **c**, **d**, Pump-wavelength tuning of the FM-OPO driven with  $M/2\pi \approx 100$  MHz, and 510 MHz, respectively. All measurements in **b**, **c**, and **d** correspond to pumping

the device with about 140 mW of optical power. The faint line in the center of each colormap corresponds to the FH pump leakage into the cavity. **e**, FM-OPO can be driven with the RF frequency on resonance with the cavity FSR near degeneracy ( $\Omega = \zeta_1$ ) or detuned ( $\Omega - \zeta_1 = \delta \neq 0$ ). **f**, Tuning of the FM-OPO comb spectrum with RF detuning  $\delta$ . **g**, Total integrated comb power as a function of RF frequency and detuning  $\delta$ .

**Extended Data Table 1 | Summary of the FM-OPO device parameters**

Parameter	Units	Description	Value	Uncertainty
Average $Q_a$ ( $10^6$ )	-	Average FH quality factor, measured by laser spectroscopy of cavity at FH	1.0	0.2
Average $Q_a^{(i)}$ ( $10^6$ )	-	Average FH intrinsic quality factor, measured by laser spectroscopy of cavity at FH	1.6	0.3
$\kappa_b / (2\pi)$	GHz	Effective loss rate of the SH pump, calculated from simulated group velocity	3.566	0.008
$\eta_a$	-	Cavity escape efficiency, extracted from average $Q_a^{(e)}$ and $Q_a$	0.36	0.04
$\zeta_1 / (2\pi)$	GHz	Cavity free spectral range, measured by laser spectroscopy of cavity at FH	5.7853	0.0002
$\zeta_2 / (2\pi)$	kHz	Cavity dispersion, measured by laser spectroscopy of cavity at FH	-11.1	0.5
$\eta$	%/ $Wcm^2$	Peak waveguide nonlinear efficiency, measured on a periodically poled LN waveguide	1,500	100
$g$	kHz	Nonlinear interaction rate, extracted from fitting output power of the OPO	12	2
$M_0$	MHz/V	Electro-optically induced mode-coupling rate, fitted from modulated cavity transmission	60	1
$P_{th}$	mW	SH power threshold of the OPO, extracted from fitting output power of the OPO	47	1
$\rho_{int}$	%	Internal OPO efficiency, inferred from the SH depletion	93	3
$\rho_{max}$	%	Total OPO efficiency, inferred from the SH depletion and $\eta_a$	34	4